Dynamical study of three African Easterly Waves in September 2021

Tanguy Jonville, Cyrille Flamant, Christophe Lavaysse

Received: 20 July 2023 | Revised: 29 December 2023 | Accepted: 22 February 2024

DOI: 10.1002/qj.4720

Quarterly Journal of the Royal Meteorological Society RMetS

RESEARCH ARTICLE

Dynamical study of three African Easterly Waves in September 2021

Tanguy Jonville[1,2] | **Cyrille Flamant**[1] | **Christophe Lavaysse**[3,4]

[1]Laboratoire Atmosphères, Milieux, Observations Spatiales, CNRS-SU-UVSQ, Paris, France

[2]Ecole des Ponts, Marne la Vallée, France

[3]Institut des Géosciences de l'Environnement, CNRS-UGA-INRAE-IRD-Grenoble INP, Grenoble, France

[4]Joint Research Centre, European Commission, Ispra, Province of Varese Italy

Correspondence
Tanguy Jonville, LATMOS, Sorbonne Université Campus Pierre et Marie Curie, 4 place Jussieu, Paris, 75252, France.
Email: tanguy.jonville@latmos.ipsl.fr

Funding information
Ministère de la Transition écologique et Solidaire; Centre National d'Etudes Spatiales; European Space Agency, Grant/Award Number: RFP/3-16595/20/NL/FF/ab; Institut Pierre-Simon Laplace; Institut National des Sciences de l'Univers (INSU) of Centre National de la Recherche Scientifique (CNRS)

Abstract

Three convectively active African easterly waves (AEWs) that propagated south of the African easterly jet were observed over the northeast Atlantic Ocean in September 2021. Their evolution is studied using a suite of theoretical frameworks, as well as the European Centre for Medium-range Weather Forecast reanalyses and satellite-derived brightness temperature observations. The environment of these AEWs was sampled during the Cloud–Atmospheric Dynamics–Dust Interactions in West Africa campaign near Cape Verde with the goal to assess their potential for developing into tropical cyclones. We highlight the processes that inhibited the development of the first AEW (which evolved into tropical disturbance *Pierre-Henri*) and that played a role in the development of the later two into tropical storms *Rose* and *Peter* on September 19, 2021. The three AEWs developed a so-called "marsupial protective" pouch. For *Peter* and *Rose*, the pouch was associated with a vertically aligned vortex at low levels and efficiently protected the convective systems inside from dry and dusty air intrusion. The development of this low-level vortex is associated with an interaction with the monsoon trough for *Rose* and with a vorticity center associated with a wave propagating north of the African easterly jet (AEJ) in the case of *Peter*. The presence of a dust flux toward the convective core near the surface is highlighted for *Rose* and *Peter* in spite of the presence of the protective marsupial pouch. On the other hand, *Pierre-Henri* interacted positively with both the monsoon trough and an AEW north of the AEJ but failed to develop into a tropical cyclone. The wave north of the AEJ brought Saharan air layer air masses inside the pouch that led to a drying of the circulation that may explain the decrease in convective activity.

KEYWORDS

African easterly waves, deep convection, dust, monsoon trough zone, tropical cyclones, tropical storms

1 | INTRODUCTION

African easterly waves (AEWs) are mixed barotropic–baroclinic instabilities. They are characterized by a period of 2–10 days and wavelengths of 2000–3000 km (Burpee, 1972; Thorncroft et al., 2008) and are known to modulate precipitation and convection over West Africa (Cornforth et al., 2009; Fink & Reiner, 2003; Mekonnen et al., 2006) and to interact with the West African monsoon circulation (Lavaysse et al., 2010). They propagate along two wave tracks, north and south of the African easterly jet (AEJ). They have long been associated with tropical cyclogenesis (Brammer & Thorncroft, 2015; Chen, 2006; Chen et al., 2008; Enyew & Mekonnen, 2022; Leppert et al., 2013; Russell et al., 2017; Thorncroft & Hodges, 2001). Russell et al. (2017) estimate that nearly 70% of named tropical cyclones (TCs) in the Atlantic and 80% of hurricanes are linked to an AEW. Even though the causal links between AEWs and TCs are still subject to debate—Patricola et al. (2018) showed, for example, that cyclonic activity remains unchanged by removing the activity of AEWs in their simulations—AEWs modulate the timing and location of cyclonic events (Danso et al., 2022). They are monitored by the National Oceanographic and Atmospheric Administration's National Hurricane Center (NHC) in its "Atlantic Tropical Cyclones and Disturbances" short-term forecast reports. The development of an AEW into a TC is, however, still poorly understood, as only about 15% of AEWs develop into TCs.

One of the most promising frameworks to understand the interaction between AEWs and TC genesis is the "marsupial paradigm" framework (Tang et al., 2020). It was put forward by Dunkerton et al. (2009) and can be depicted as follows: in the frame of reference of the wave trough, if the wave center is close to its critical layer (the latitude at which the mean flow equals the phase speed), a sweet spot for genesis is formed. It is marked by closed streamlines that define a "Kelvin cat's eye" or wave pouch; that is, a region protected from outside air intrusion and that moves at wave speed. This region is particularly favorable for the development of a TC. It will be moistened by convection and surface moisture fluxes, it is protected from lateral intrusion of dry air in the low- to mid-troposphere, and it benefits from the cyclonic preconditioning of the wave trough. In turn, the wave can be invigorated by the energy liberated. If the pouch is maintained long enough for mesoscale convective systems (MCSs) to develop, they can intensify enough to be self-sustained and become a TC (Dunkerton et al., 2009).

This analysis framework has been effectively used for several case studies (Tang et al., 2020), and especially in the North Atlantic basin on AEWs (Asaadi et al., 2016a, 2016b; Rutherford et al., 2018; Wang et al., 2010a). Between 1998 and 2001, Asaadi et al. (2017) found that only 25% of AEWs were associated with the formation of a Kelvin cat's eye. In particular, all AEWs that were linked to a TC genesis presented such a configuration, compared with only 10% of non-developing AEWs. Wang, Dunkerton, and Montgomery (2012) argued that the development of a deep pouch might be a sufficient criterion for genesis if associated with the environmental context (large-scale sea-surface temperature [SST], wind shear, and water content). The dynamical characteristics of the pouch itself play a role in its further development or decay. The vertical coherence of the pouch may be a key factor, as it is associated with strong rotation and weak wind shear (Montgomery et al., 2010; Wang et al., 2010a, 2010b). Brammer et al. (2018) studied an intense AEW that presented a pouch-like structure at jet level, but the lack of alignment between the jet level and low-level circulation leads to significant intrusion of dry air that might have prevented genesis. On the other hand, a vertical alignment of the vortex associated with the pouches is observed in the hours before TC genesis for every AEW associated with a TC (Wang & Hankes, 2014) and low-level kinetic energy is a good predictor of TC activity (Russell et al., 2017). It may also help the AEW to transition thermodynamically: as has been put forward by Jenkins (1995), AEWs are associated with a cold anomaly at jet level produced mainly by the thermal-wind balance and associated with the gradient of vorticity between the altitude of the jet where the wave peaks and the lower troposphere where little to no vorticity anomaly is observed. The supply of vorticity at low level thus warms the core of the circulation, which has been identified to be an important step toward TC genesis (Tang et al., 2020).

An extension of the vortex from the jet level toward the lower troposphere is observed in most AEWs of the south track as they leave the coast in relation to the land–ocean transition and with an increased coupling between the wave and convective activity (Janiga & Thorncroft, 2013; Mekonnen et al., 2006). The low-level vortex can be effectively invigorated when an AEW passes over the region where the monsoon flow meets the northeasterly trade winds over the ocean (Arnault & Roux, 2010, 2011). This region is associated with positive vorticity in the low troposphere, low-level convergence, and a negative pressure anomaly and will be hereby referred to as the monsoon trough by analogy with the Asian monsoon trough. AEWs that develop into TCs are associated with a more intense monsoon flow and deeper wave pouches (Ocasio et al., 2021). The merging of vortices on the south and north wave tracks can also significantly invigorate the low-level vortex and favor TC genesis, as the activity of the northern wave track peaks at lower altitudes (Arnault & Roux, 2011; Duvel, 2021; Hankes et al., 2015).

In West Africa and in the North Atlantic, Saharan dust interacts with atmospheric dynamics and cloud physics. However, no comprehensive framework articulates the impact of dust, and the formation of the marsupial pouch and dust-related effects are still a major source of uncertainty in climate and weather prediction models (Baklanov et al., 2018; Seinfeld et al., 2016). In the boreal summer, dust is emitted by dry convection and winds over the Sahara and is advected over the Atlantic by the AEJ, resulting in the formation over the ocean of a distinct, elevated, dust-laden, dry and warm layer known as the Saharan air layer (SAL). It has a strong radiative impact on its environment by increasing static stability where dust is located (Reale et al., 2014) and decreasing SST below, thereby affecting cyclogenesis (Pan et al., 2018; Sun & Zhao, 2020) and the monsoon circulation (N'Datchoh et al., 2018; Sun & Zhao, 2020). The impact of the SAL on the growth of AEWs is still debated (Grogan et al., 2016; Jones et al., 2004; Jury & Santiago, 2010) as dust transport in the SAL is modulated by AEW activity (Grogan et al., 2019; Knippertz & Todd, 2010; Nathan et al., 2019). Furthermore, dust may also have indirect effects on AEW dynamics and cyclogenesis, as terrigenous aerosols are efficient ice-nucleating particles (INPs) that can impact the nature of deep convective clouds (Fan et al., 2016; Saleeby et al., 2015). They may favor the transition of AEWs from cold core to warm core perturbations through the liberation of latent heat (Kwon & Mak, 1990). Aerosols have also been found to have a significant impact on TC intensity (Herbener et al., 2014; Rosenfeld et al., 2012) and trajectory (Hoarau, 2018; Nowottnick et al., 2018).

The multiscale nature of the processes at stake makes their modeling particularly challenging. The spatial observation of the processes is hindered by the opacity of the cloud layers that are collocated with them. It is in this context that the Cloud–Atmospheric Dynamics–Dust Interactions in West Africa (CADDIWA) campaign was held in September 2021 (Flamant et al., 2021, 2024). Its objective was to study the interactions between clouds, dust, and atmospheric dynamics in West Africa, and especially to assess the relative contributions of direct, semi-direct, and indirect radiative effects of aerosols in the region and their impacts on cyclogenesis. The observations were carried out through the deployment of the French Falcon 20 environmental research aircraft of Safire (Safire FA20) from the Amilcar Cabral International airport on Sal island, equipped with radar and lidar systems, dropsondes, and micro-physical probes. The airborne data were supplemented by radiosondings also launched from the airport on Sal island. Three AEW troughs were sampled during the campaign. The first passed over Sal on September 11–12 but failed to develop into a TC. It only grew to become a tropical disturbance, referred to as *Pierre-Henri* (named by the campaign team and in all campaign papers, as in the following, in memory of Pierre Henri Flamant; see (Flamant et al., 2024)). The latter two traveled south of Cape Verde and developed into the tropical storms *Peter* and *Rose* on September 19.

This study is based on the fifth-generation European Centre for Medium-Range Weather Forecast Reanalysis (ERA5; (Hersbach et al., 2020)) and Copernicus Atmospheric Monitoring Service (CAMS; (Inness et al., 2019)) reanalysis and satellite data. The aim is threefold: (a) to understand the dynamical processes that led to the development of *Rose* and *Peter* and prevented the development of *Pierre-Henri*; (b) to test the marsupial paradigm framework, as well as the hypothesis of monsoon–wave interaction and of north–south waves interaction on those three case studies; and (c) to pave the way for future studies on the cloud–atmospheric dynamics–dust interactions in September 2021. After a presentation of the synoptic context of September 2021, the three AEWs will be studied within the marsupial paradigm framework. Interaction with the monsoon and between north- and south-track waves will be discussed. Eventually, the impact of the wave pouch on dust transport inside the circulation will be highlighted.

2 | DATA

All thermodynamical products used in this study come from ERA5. The reanalysis has a 1 h temporal resolution and is based upon the atmosphere dynamic model IFS Cy41r2, applied on a grid with a 31 km horizontal resolution. It has 137 vertical levels from the ground to 1 Pa. To properly take into account the interactions with the sea surface, the atmosphere model is coupled with a wave model with 0.36° spatial resolution (Hersbach et al., 2020). The data used for this study are regridded on ERA5 37 pressure levels on downloaded for every 6 h. Temperature, humidity, and horizontal wind speed have been validated against the campaign dropsondes and radar data (not assimilated) for their use in the region of interest (see Supporting Information). Aerosol concentrations are deduced from CAMS reanalysis. It is based on the last release to date of the atmosphere dynamic model IFS (Cy42r1), and the same meteorological observation dataset as in ERA5 is assimilated (Inness et al., 2019), maintaining a high level of consistency between the two datasets.

Convective activity is diagnosed using brightness temperature from the MERGED-IR dataset, a 4 km–30 min interpolation of merged infrared data from the Geostationary Operational Environmental Satellite, METEOSAT, and Geostationary Meteorological Satellite-5/Multifunctional

Transport Satellite-1R/2/Himawari-8 geostationary satellites (Janowiak et al., 2017).

Finally, NHC best-track data were used in this study to estimate the location of a TC genesis and to determine whether the TC is related to an AEW. Best-track data are widely used in the literature and constitute a dataset of reference. The coordinates of the perturbation centers have been especially deemed to have a satisfying accuracy, though the uncertainty decreases with increasing intensity, making the dataset less reliable for the early stages of development (Landsea & Franklin, 2013).

3 | SEPTEMBER 2021 CONTEXT: TROPICAL CYCLOGENESIS INDEX AND WAVE ACTIVITY

Figure 1a,c shows monthly means of SST, relative humidity (RH) at 850 hPa, wind shear between 200 and 850 hPa, and vorticity at 850 hPa across the tropical Atlantic and African continent north of the Equator for September 2021. Also shown are the anomalies of these fields with respect to the climatology (Septembers between 1991 and 2021; Figure 1b,d). In September 2021, the ocean is significantly warmer than the climatology, especially to the south of the basin and close to the South American and sub-Saharan coasts. The anomaly is the weakest at 15°N and in the center of the basin. A cold tongue can be observed in the SST anomaly, in the wake of Hurricane *Larry* (see Figure 1g). It is likely related to the mixing induced in the ocean by the wind-forced circulation. Emanuel (2001) has already discussed the cooling of the surface ocean due to the Ekman pumping induced by TCs. Positive anomalies of RH at 850 hPa are collocated with a strong positive anomaly of SST. The middle of the basin is characterized by drier conditions.

The wind shear is greater than the climatology in the whole Atlantic basin in September 2021 and is a minimum in the center of the basin. The 850 hPa vorticity field in September 2021 is characterized by (a) a strong signature of hurricanes *Larry* and *Sam*, and (b) a positive anomaly south of 15°N between 40°W and the coast that is thought to be related to a strong AEW activity on the southern flank of the AEJ.

Those synoptic characteristic of September 2021 have opposite effects on tropical cyclogenesis. On the one hand, stronger ambient cyclonic vorticity and higher SST may favor TC development. On the other hand, strong wind-shear will likely inhibit the vertical development of TCs, and drier conditions may be detrimental to deep convection. To aggregate those products, we use the monthly genesis potential index defined by Tippett et al. (2011). It has proven to be better correlated to TC activity than the other monthly genesis potential indices over the Atlantic in the comparative study of Menkes et al. (2012). The Tippett genesis potential index (GPI) is defined as follows:

$$\mu = \exp(b + b_\eta \min(\eta, \eta_0) + b_\mathcal{H}\mathcal{H} + B_T T + b_V V + \log\cos\phi), \quad (1)$$

where η (s^{-1}) is the relative vorticity at 850 hPa, $\eta_0 = 3.7 \times 10^{-5}\,s^{-1}$, $\mathcal{H}$ (%) is the RH at 600 hPa, T is the relative SST, defined as the SST minus the mean SST between 20°S and 20°N, and V is the wind shear between 200 and 850 hPa. Tippett et al. (2011) define the value of the coefficient as $b = -5.80$, $b_\eta = 1.03 \times 10^5$ s, $b_\mathcal{H} = 0.05$, $b_T = 0.56\,K^{-1}$, and $B_V = 0.15\,s{\cdot}m^{-1}$ based on a Poisson regression.

Figure 1e,f shows the results. A wide region of potential for TC development across the whole basin is highlighted between 7 and 15°N (Figure 1e). The GPI in September 2021 is seen to be weaker than the climatology (Figure 1f), which might explain why no TC reached the hurricane stage in mid-September, after Hurricane *Larry*. A signature of Hurricane *Sam*'s trajectory (see Figure 1f,g) is still visible on the western side of the basin, mainly due to the fact that the 850 hPa relative vorticity associated with the storm dominates the monthly mean and is passed as an argument of GPI calculation, overriding every other feature in the region of development of *Peter*.

Relative to the two other cases, *Peter* develops in the most favorable region; it benefits from positive anomalies of SST and RH and from a moderate wind shear compared with the rest of the area. *Rose*, on the other hand, develops in a region with no anomaly of SST nor of ambient vorticity, but in a region of positive anomaly of wind shear and negative anomaly of RH. The location where it develops is at the northernmost point of the area of favorable development and has a lower GPI than the climatology. It is thus expected that shorter time-scale processes will be even more important for *Rose* as they will have to counteract moderately unfavorable conditions. As for *Pierre-Henri*, it fails to develop but reaches its maximum kinetic energy over a region with a positive anomaly of SST, a negative anomaly of ambient vorticity, in an environment slightly drier and with a moderate wind shear compared with the rest of the region. The region in which *Pierre-Henri* reaches its maximum kinetic energy is less favorable to genesis than in the climatology.

Now that we have introduced the synoptic context, we analyze the dynamics of the AEWs. A wavelet decomposition of the meridional component of wind is performed to highlight the frequency windows active in September 2021, as well as the evolution of AEW amplitude with respect to time using PyWavelet (Lee et al., 2019). Consistent with the guidelines of Torrence and Compo (1998), a complex Morlet wavelet is chosen. The power density

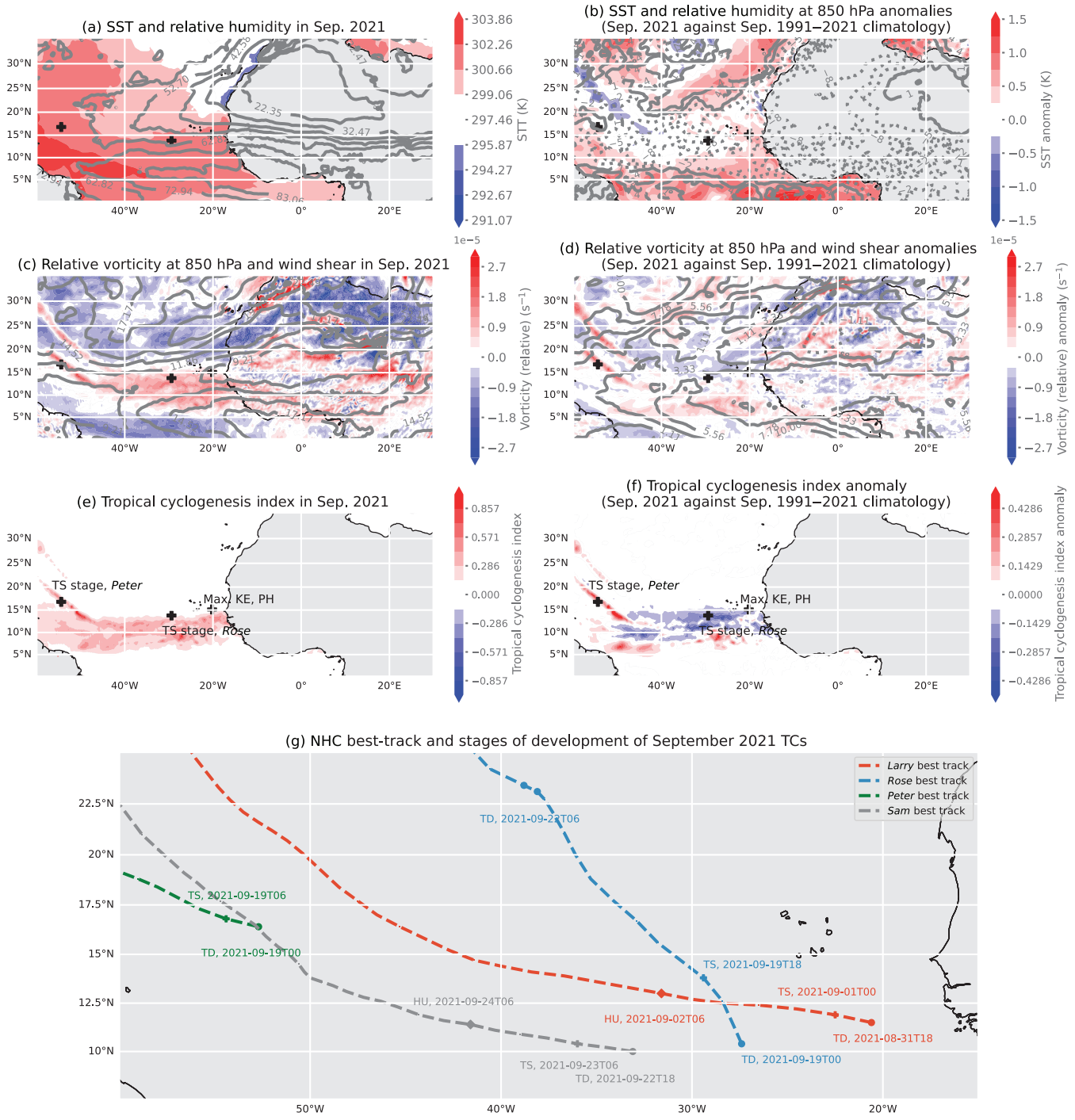

FIGURE 1 (a) Averaged sea-surface temperature (SST; shading, K) and relative humidity at 850 hPa (contours, %) for September 2021. (b) Same as (a), but for September 2021 anomalies compared with the 1991–2021 climatology for September. (c) Averaged relative vorticity (shading, s^{-1}) and 850 hPa − 200 hPa wind shear (contour, $m \cdot s^{-1}$) for September 2021. (d) Same as (c), but compared with 1991–2021 September climatology. (e) Tippet genesis potential index computed for September 2021. KE: kinetic energy; PH: *Pierre-Henri*; TS: tropical storm. (f) Same as (e), but compared with 1991–2021 climatology. The two westernmost black crosses mark *Rose* and *Peter* genesis according to the National Hurricane Center (NHC) best-track data; the easternmost cross marks the location where *Pierre-Henri* reached its maximum integrated 750–1000 hPa KE (summed over the region defined by ±3° of latitude and longitude around the vorticity center). (g) NHC best-track data and stages of development for September 2021 tropical cyclones (TCs). HU, hurricane; TD, tropical depression.

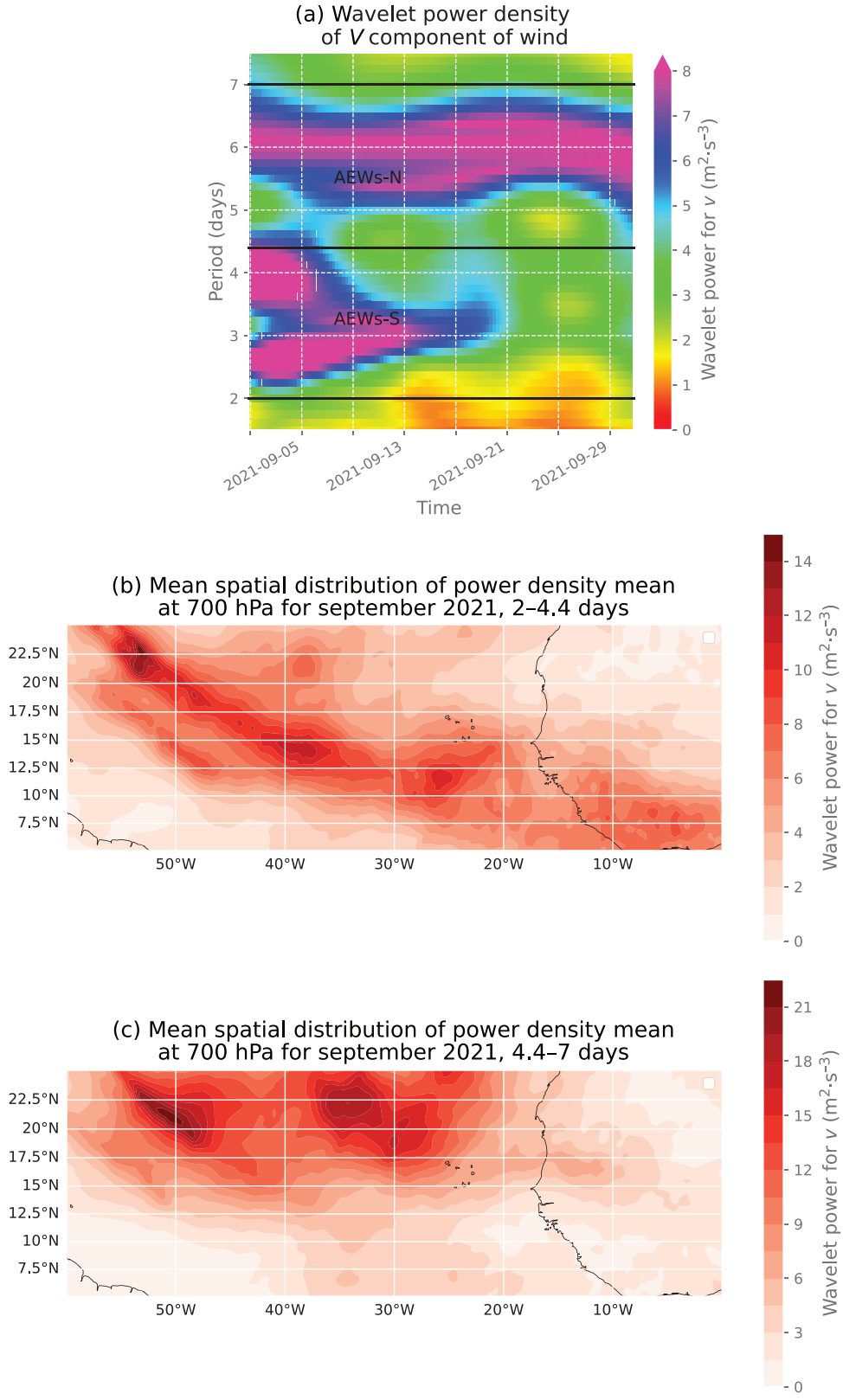

FIGURE 2 (a) Mean of wavelet decomposition of the meridional component of the wind between 60°W and 0°W and between 5°N and 25°N in September 2021. AEWs: African easterly waves. (b) Power density for the 2–4.4 days period window averaged for September 2021. (c) Power density for the 4.4–7 days period window averaged for September 2021.

is then computed by dividing the modulus of each coefficient by the central frequency of its associated wavelet, consistent with the method of Liu et al. (2007). Mean results over the region of development and growth of AEWs (40°W–20°E, 5°N–25°N) are shown in Figure 2a. On the frequency window commonly used to study AEWs (2–7 days), two peaks can be distinguished: a first between 2 and 4.4 days, active between September 1 and 21,

and a second peak between 4.4 and 7 days, active from September 5 onward. The geographical distribution of power density associated with each peak is shown on the panel b and c. As is shown in Figure 2b,c, each peak is active in a different region. East of 40°W, the 2–4.4 days mode is mainly active south of 15°N and presents a southeast–northwest tilt, whereas the 4.4–7 days mode is active north of 15°N and is more zonal. Those characteristics are consistent with the description of the two wave tracks north and south of the AEW. The 2–4.4 days mode is associated with south track activity and the 4.4–7 days mode with north wave activity.

We track each vorticity center to study the evolution of the vortices associated with the three AEWs. AEWs present multiple vorticity centers when filtering on the 2–7 days period window in the September 2021 vorticity signal, with different phase speed and trajectory discontinuity (not shown here). These discontinuities might be the result of a merger or interaction of the north- and south-track waves, such as those discussed by Hankes et al. (2015) or Duvel (2021). To highlight north–south vortex interaction, and have more robust trajectories, the tracking is done by following filtered vorticity centers on the 2–4.4 days period scale. Those are furthered referred to as AEW-S. Vorticity centers south of the AEJ (AEW-S) are tracked similarly on the 4.4–7 days period scale. The fact that the two spectrum peaks are spectrally exclusive (see Figure 2a) and the presence of a buffer of little to no activity between the two peaks ensures that the pollution of one mode by the other is limited. A Hovmöller plot for the period of the campaign is shown in Figure 3. The 700 hPa vorticity, filtered on the 2–4.4 days window and averaged between 5°N and 20°N is shown in shading. The 700 hPa vorticity filtered on the 4.4–7 days window is shown in contour. The three AEW-S vortices sampled during the CADDIWA campaign can easily be identified at 23°E on September 13 (*Pierre-Henri*), September 15 (*Peter*), and September 18 (*Rose*). The trajectories obtained by the tracking of the vortices are plotted in Figure 6, and in Figure 3 to show their consistency with the Hovmöller.

AEWs-N display slightly longer wavelengths than AEWs-S do, and a significantly smaller phase velocity. This difference in characteristics between AEWs-N and AEWs-S has already been discussed—for instance, see Pytharoulis and Thorncroft (1999)—and the findings of the literature are consistent with our results. One possible explanation for those structural differences is the nature of the underlying genesis and growth processes: whereas baroclinic processes are predominant for AEWs-N, the dominant growth process of AEWs-S is of barotropic exchanges with the AEJ (Diaz & Aiyyer, 2013; Thorncroft, 1995) resulting in quicker phase velocity. According to Pytharoulis and Thorncroft (1999), AEWs-N also peak at a lower altitude than AEWs-S do. This is also the case

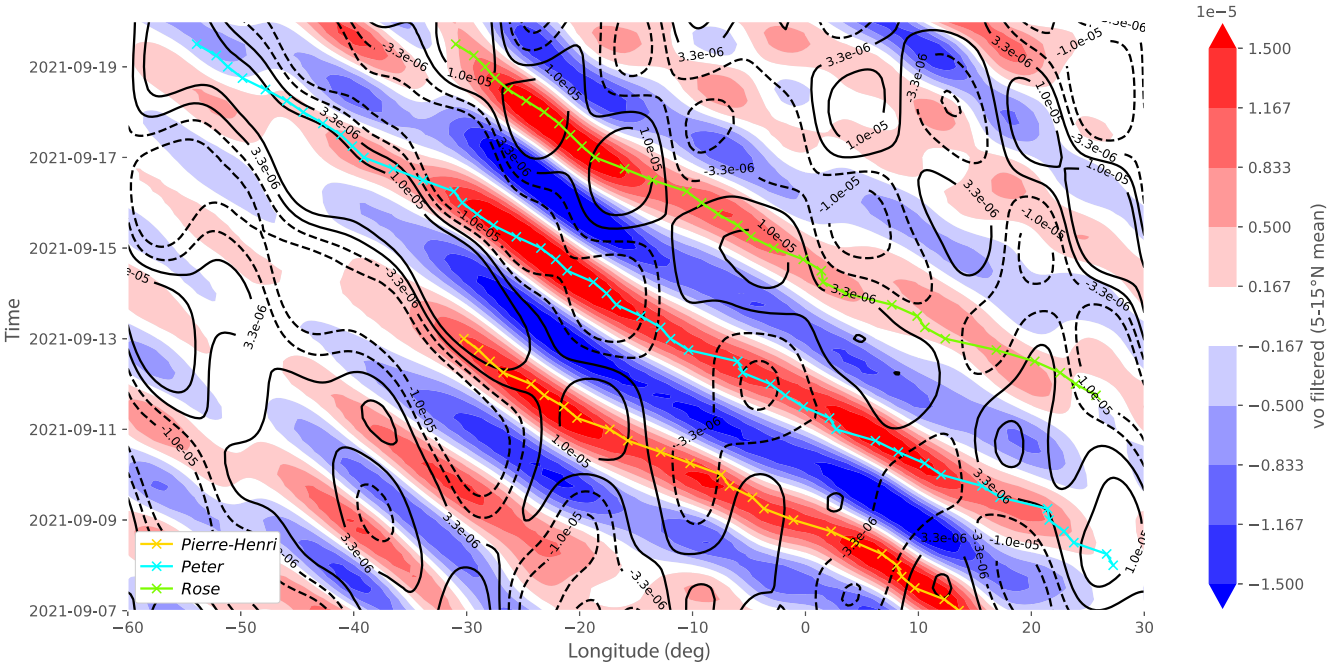

FIGURE 3 Hovmöller of filtered relative vorticity at 700 hPa. Frequency and latitude windows: 2–4.4 days, 5–15°N in shading, 4.4–7 days, 15–25°N in black contours. The trajectory of the African easterly waves-S associated with *Pierre-Henri*, *Peter*, and *Rose* are shown in color. Mean phase speed of 2–4.4-day waves: 9.1×10^2 km·day^{-1}. Mean phase speed of 4.4–7-day waves: 4.4×10^2 km·day^{-1}.

for the two AEW-N troughs (first one observable at 10°W and second one at 25°E on September 7) observed during the campaign that are associated with a maximum relative vorticity at 800 hPa or lower (figures not shown). Those structural differences may result in wave–wave interactions that may play a role in the transition of AEWs to TCs. For instance, an intensification of the circulation and of its vertical extension may be expected when an AEW-N and an AEW-S interact, as will be discussed in the following sections.

4 | THE MARSUPIAL PARADIGM

The presence of a pouch within an AEW has been identified as a key step toward genesis. Several diagnostics have been used in the literature. A common way to identify the potential location of a pouch is to look for the intersection between the trough axis (where $v = 0$) with the critical layer (isoline $u = 0$ in the frame of the trough) (Dunkerton et al., 2009; Montgomery et al., 2012; Wang & Hankes, 2014). The Okubo–Weiss parameter, or the product of the Okubo–Weiss parameter with relative vorticity, has been used by Dunkerton et al. (2009), Tory et al. (2013), and Rutherford et al. (2018) to identify whether a pouch has effectively developed. Finally, filtered potential vorticity (PV) has been used by Asaadi et al. (2016a, 2016b, 2017) to identify the pouch. In the following, we will use the intersection of the trough axis and the critical layer and the potential vorticity as means of identifying the pouch.

The filtered PV distribution—333 km running mean, same spectral resolution as in (Asaadi et al., 2016a) and Asaadi et al. (2016b)—at 700 hPa, brightness temperatures, and streamlines in the frame of reference of the AEW-S trough associated with the circulation, as well as the critical layer and the trough axis, are shown in Figure 4 for *Pierre-Henri* and in Figure 5 for *Rose* and *Peter*. For *Pierre-Henri*, the presence of the pouch is shown for dates ranging from the day when the peak of kinetic energy was reached (figure not shown) until September 11 at 1800 UTC, before the MCS dissipates. MCSs are hereby defined as contiguous cloud-covered areas with one ore more active convective cells, identified by low brightness temperature. At the date of the maximum kinetic energy, the PV at 700 hPa shows moderate value (<0.4 PVU). The streamlines collocated with the most active MCSs are not closed and come through the dusty air mass characteristic of the SAL. The PV pouch eventually intensifies on September 11, but the convective activity has already decreased. Moreover, the closed streamlines on September 11 enclose part of the SAL: dry air is captured inside the pouch. If dry air is enclosed in the Kelvin cat's eye, the processes described in introduction are inhibited (Wang et al., 2010a). Brammer et al. (2018) already documented the case of a non-developing wave wrapping around a dry air mass initially in its northwestern quadrant, in

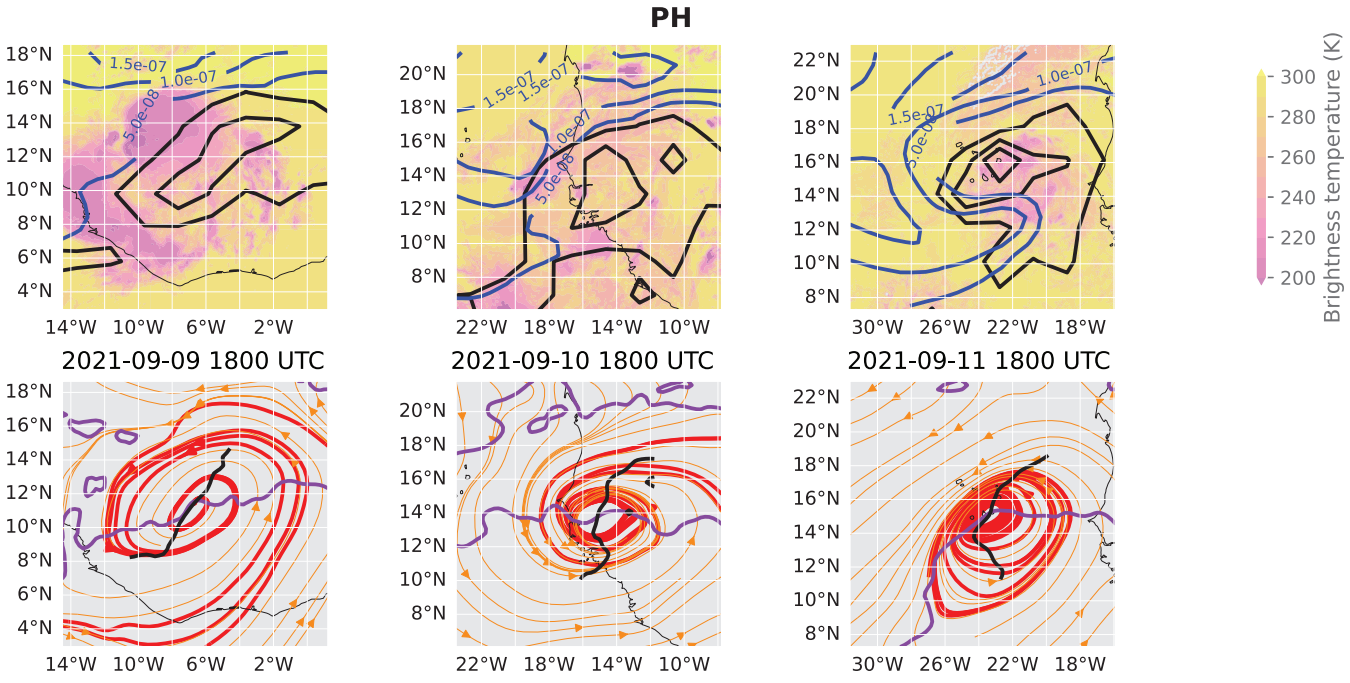

FIGURE 4 Top: Potential vorticity at 700 hPa (thick black contour, one line each 0.2 PVU), brightness temperature contour (shading), dust concentration (blue contours). Bottom: Streamlines in the frame of reference of the vorticity center associated with *Pierre-Henri* (PH) at 700 hPa (orange and red), trough axis (thick black line), and critical layers (purple lines).

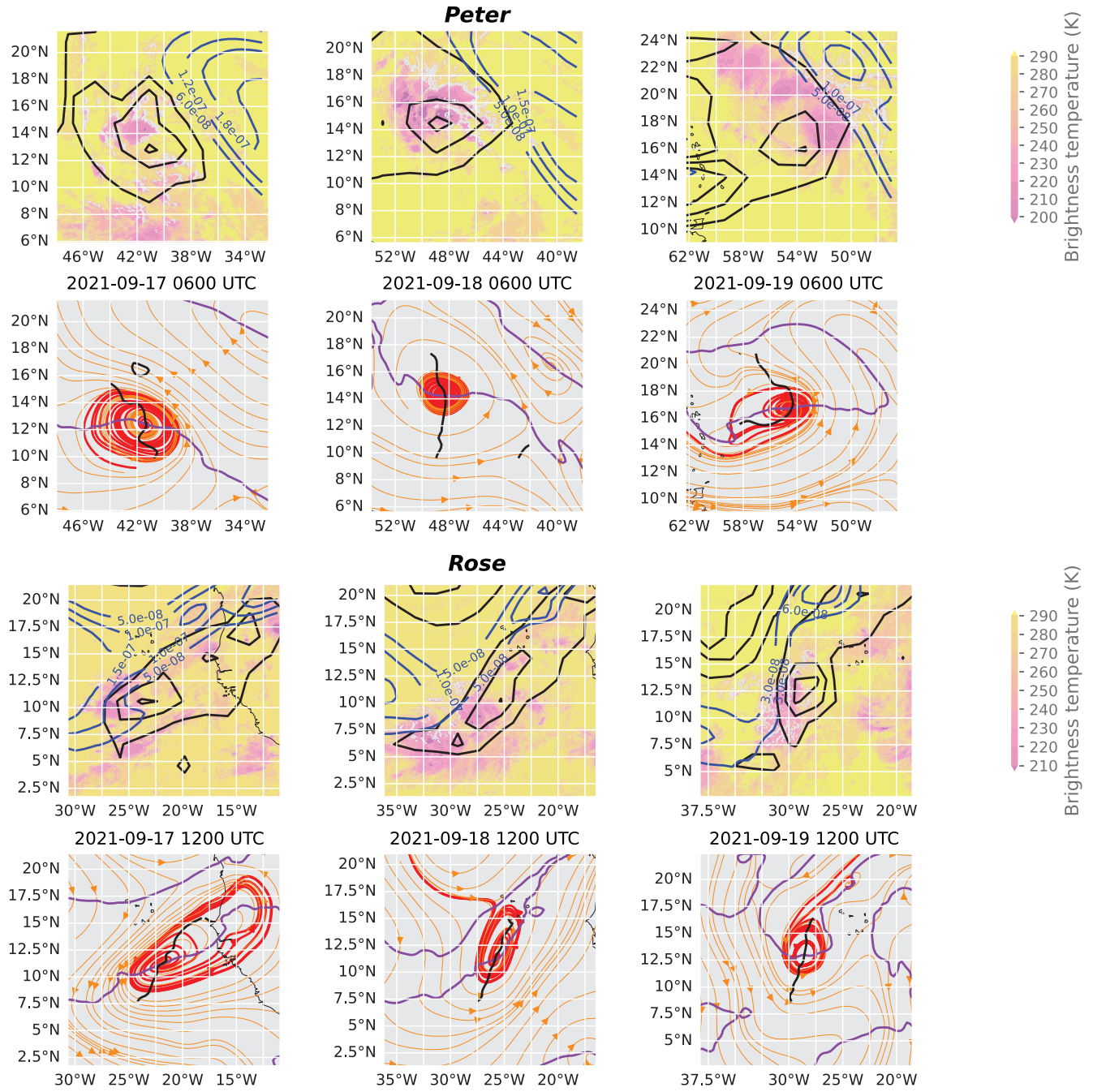

FIGURE 5 As Figure 4, but for *Peter* (top) and *Rose* (bottom). Light red streamlines denote streamlines seeded in the convective system out of the Kelvin cat's eye.

correlation with a misaligned vortex at low levels. We will explore this hypothesis in the following sections.

For *Rose* and *Peter*, Figure 5 shows the results 48 h before genesis, 24 h before genesis, and at the date at which the circulation reaches the TS stage. For those two cases, the signal of PV show an intense pouch (>0.6 PVU) collocated with MCSs at the crossing of the wave trough and the critical layer 48 h before the genesis. Streamlines are closed or quasi-closed around one or part of one MCS and do not enclose dusty air characteristic of the SAL. MCSs out of the Kelvin cat's eye are subject to open circulations (light red streamlines) in the frame of the trough and tend to dissipate (see the large convective system south of the pouch on September 17 for *Peter* for instance, or the convective systems southwest of the pouch for *Rose* on September 18). This is consistent with the findings of Montgomery et al. (2012), who observed that deep convection outside or on the edge of the pouch experiencesmore strain and shear that are detrimental to its development than the convective system inside. This supports the hypothesis of Dunkerton et al. (2009).

5 | INTERACTION WITH THE MONSOON TROUGH ZONE

According to Wang, Montgomery, and Fritz (2012), the vortex associated with the marsupial pouch needs to be deep enough and vertically aligned for TC genesis to occur. The mixed barotropic instability that drives the growth of the AEWs over the continent is unlikely to be sufficient to explain the development of the low-level vortex over the continent. AEWs that develop into TCs propagate in mainly stable or neutral conditions over the ocean, with no change of the meridian PV gradient sign in zonal average (Asaadi et al., 2017). Baroclinic/batropic processes are found to decrease over the ocean (Diaz & Aiyyer, 2013). Barotropic conversion of energy may even reverse at the exit of the continent, the AEJ taking up energy from the AEWs (Diaz & Aiyyer, 2013; Leroux et al., 2010). Other synoptic processes may take over: interactions with the monsoon trough (Arnault & Roux, 2011; Ocasio et al., 2021) and between AEW-N and AEW-S (Duvel, 2021; Hankes et al., 2015) have been found to favor the set-up of a low-level circulation associated with the wave. This section focuses on interaction with the monsoon, and the next one on AEW-S–AEW-N interactions.

Figure 6 shows the averaged zonal wind in September 2021 with a highlight on weak wind speed indicating a change of sign for u. The zone where an AEW-S may interact with the monsoon trough is hereby referred to as the monsoon trough zone (MTZ). As expected, the MTZ can be easily identified between 42°W and 18°W and between 7.5°N and 16°N. It is marked by the black box in the figure. The three AEW-S vortices associated with *Pierre-Henri*, *Peter*, and *Rose* do go through the MTZ and could benefit from a low-level vorticity supply. However, only *Rose* develops into a TC inside the MTZ. The right panels in Figure 8 show the vertical structure of relative vorticity along each AEW-S trajectory as a function of time from the entry of the trough inside the MTZ. Whereas for *Pierre-Henri* and *Rose* a strong intensification of low-level circulation is observable, the AEW-S associated with *Peter* only displays a weak vertical extension.

In Figure 7, the low-level circulation is superimposed on the jet-level trough contours. The wave components of wind and vorticity (filtered signal with period between 2 and 7 days) are subtracted from the total signal of vorticity and winds to show the component of the low-level signal without wave activity. The blue contour lines show the isoline $u = \pm 2\,\mathrm{m{\cdot}s^{-1}}$ to delimit the region where the zonal wind sign changes, marking the transition between the trade winds and the monsoon. *Pierre-Henri* overpasses a region of moderate low-level vorticity. *Rose* evolves in a context where the isolines $-2\,\mathrm{m{\cdot}s^{-1}}$ and $+2\,\mathrm{m{\cdot}s^{-1}}$ are very close and associated with a region of strong low-level vorticity to the south of the trough center. Those two cases are comparable to the conceptual framework discussed by Arnault and Roux (2011), with a wave overpassing the positive vorticity anomaly associated with the monsoon trough. Both display an increase of vorticity in the lower levels while passing in the MTZ (see Figure 8 right panels). On the other hand, when the vortex associated with *Peter* passes over the MTZ, the trade winds and the monsoon are kept further apart than in the two previous cases by a more active and westward Saharan heat low that can be observed between the coast and 10°W at 17.5°N on September 14 and 15. The Saharan heat low disturbs the low-level circulation, creating a recirculation of westerlies at 15°N above

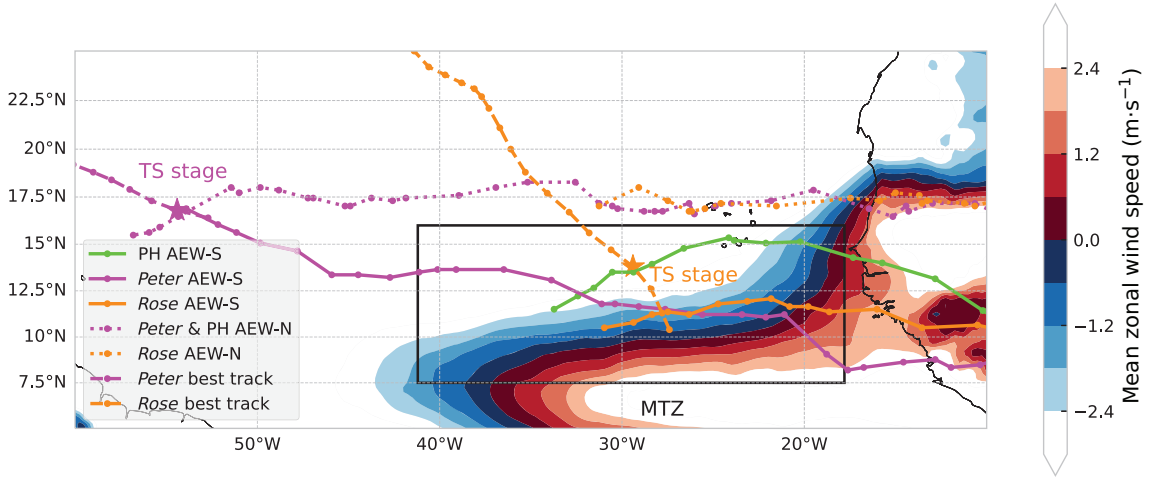

FIGURE 6 The 950 hPa zonal wind averaged over September 2021 in shading. The trajectories of the three AEWs-S, the two AEWs-N and best-track trajectories for tropical storms (TSs) *Rose* and *Peter* are shown in color. The stars mark the qualification of the circulation as a TS by the National Hurricane Center. The black box defines the monsoon trough zone (MTZ). AEW, African easterly wave; PH, *Pierre-Henri*.

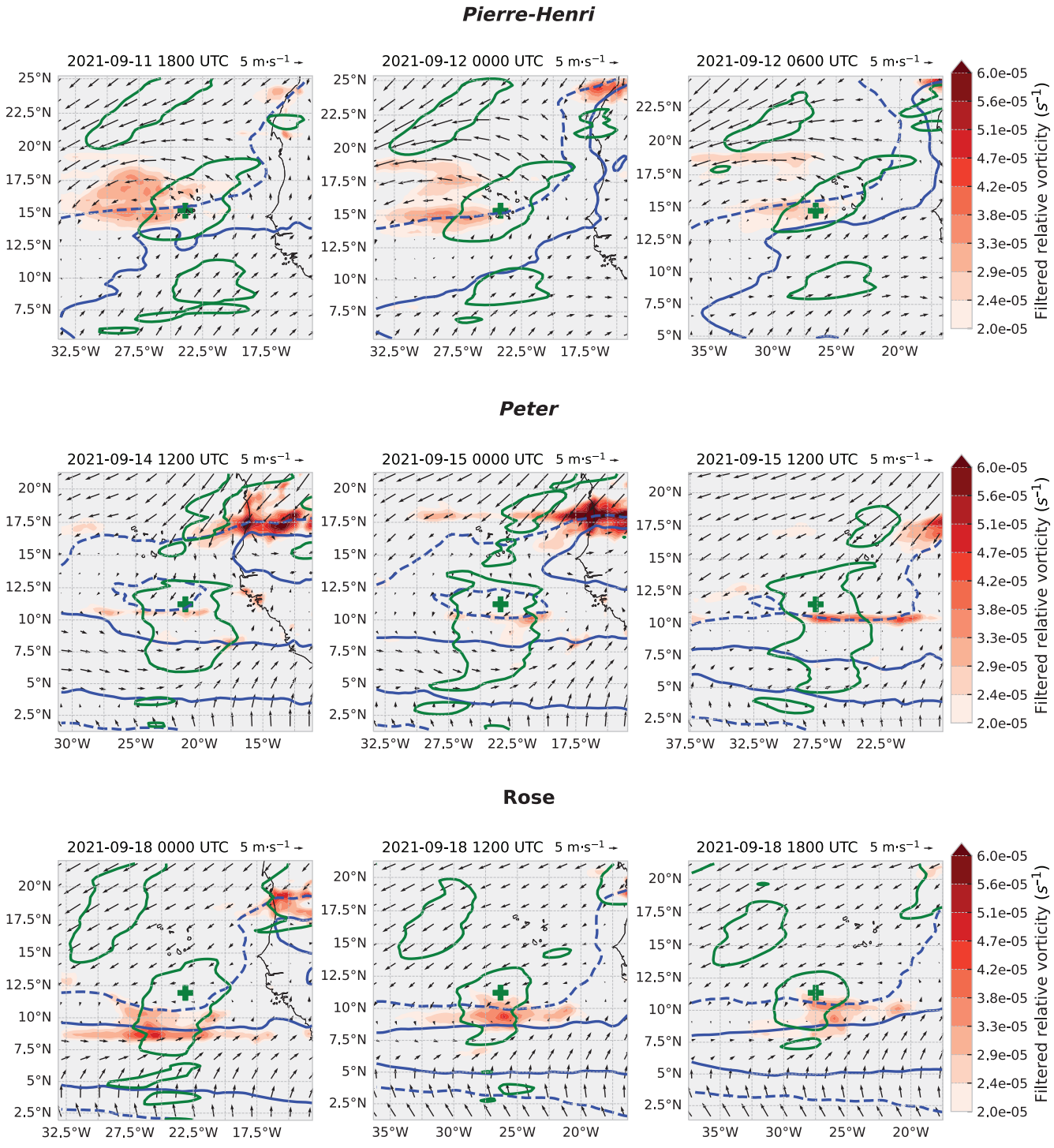

FIGURE 7 Shading: Relative vorticity at 900 hPa without African easterly wave (AEW) signals $\zeta - \zeta_{\text{wave}}$. Vector: wind at 900 hPa without AEW signals $\mathbf{u} - \mathbf{u}_{\text{wave}}$. Dashed blue line: $u - u_{\text{wave}} = -2\,\text{m·s}^{-1}$. Continuous blue line: $u - u_{\text{wave}} = 2\,\text{m·s}^{-1}$. Green contours: vorticity 700 hPa, filtered (2–4.4 days), isoline $1 \times 10^{-5}\,\text{s}^{-1}$. Green cross: tracked location of the wave center. Quantities A_{wave} are filtered on the period window 2–7 days.

the continent. Gradients of zonal winds are weakened, and only weak and limited areas of positive low-level vorticity can be observed under the jet-level vortex. After the passage of the AEW, the two isolines are closer in the whole basin. But on September 15, *Peter* is already on the edge of the westerly zone (on the right panel, the zonal component of the winds south of 7.5°N and west of 27.5°W is weak and the flow mainly to the north). The conditions are not favorable to an interaction with the monsoon beneficial for the AEW-S associated with *Peter*.

Figure 7 is purely qualitative and does not diagnose the sign of the interaction. We attempt to quantify the

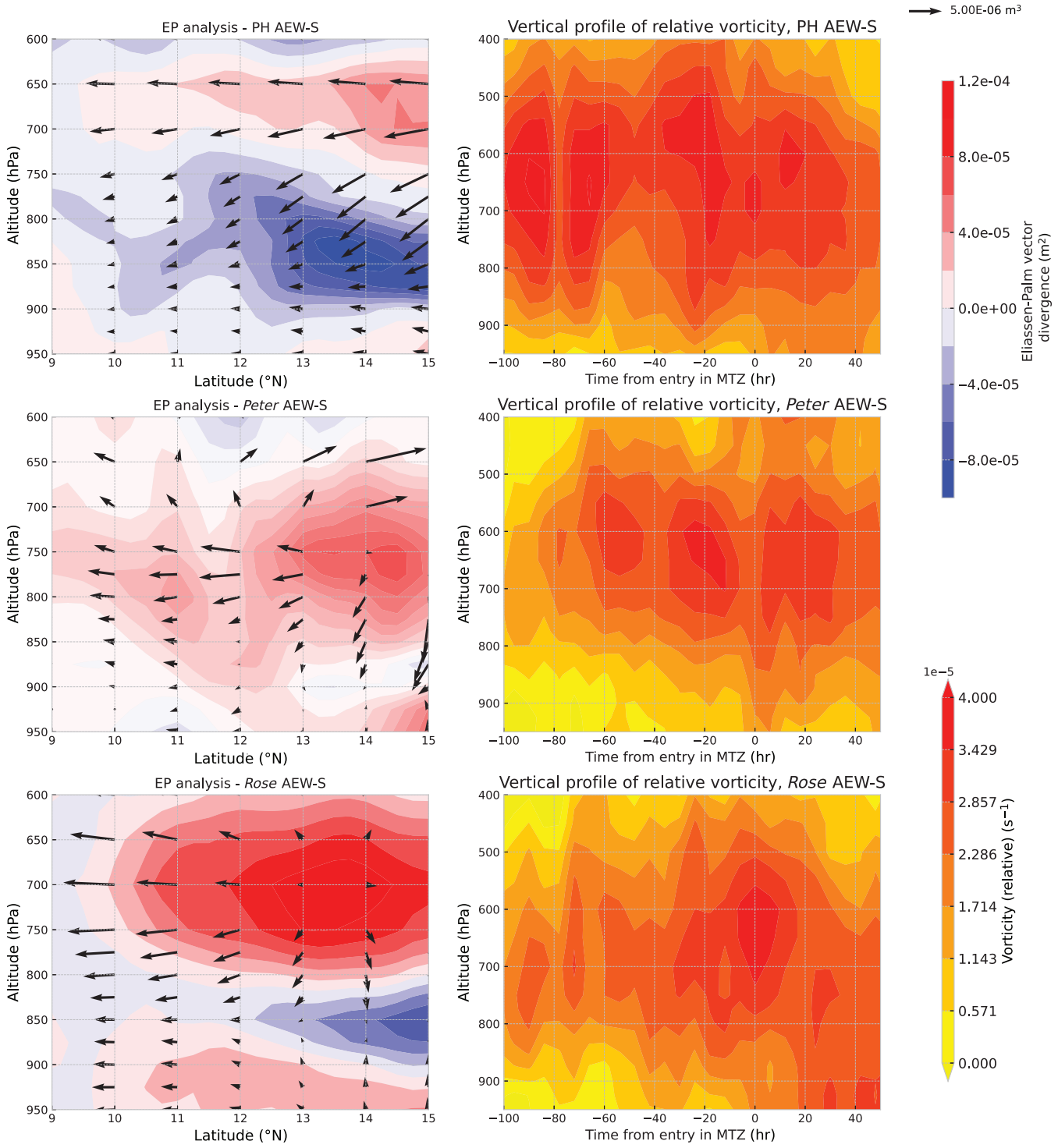

FIGURE 8 Left panels: Eliassen–Palm fluxes and corrected divergence. The Eliassen–Palm vectors are scaled as in Edmon et al. (1980), following the guidelines of the Department of Meteorology of the University of Reading (see http://www.met.reading.ac.uk/~pn904784/snap/ep&uscore;flux&uscore;calculations.htm). Right panels: Vertical profile of relative vorticity along the trajectory of the AEW-S associated with each event as a function of the time from entry in the monsoon trough zone (MTZ; in hours). AEW, African easterly wave; EP, Eliassen–Palm; PH, *Pierre-Henri*.

interaction with the MTZ by using an Eliassen–Palm decomposition. It helps in analyzing the interactions between waves in the mean flow. The Eliassen–Palm method can be derived from Boussinesq quasi-geostrophic equations in the β-plane. It is based on the decomposition of every thermodynamical quantity A into a basic state $\overline{A}$, computed as the zonal mean and considered fixed in time and a perturbation A'. The complete derivation

can be found in Vallis (2017) and leads to the equation of Eliassen–Palm, when the zonal mean is computed over the whole range of longitude:

$$\frac{\partial A}{\partial t} + \nabla \mathcal{F} = D, \tag{2}$$

$$\mathcal{F} = -\overline{u'v'}\mathbf{i} + \frac{f_0}{N^2}\overline{v'b'}\mathbf{k}, \tag{3}$$

where $A = \overline{q'^2}/(2\partial\overline{q}/\partial y)$ is the wave activity, with q the potential vorticity in the Boussinesq quasi-geostrophic hypothesis, u the zonal component of the wind, v the meriodional component of the wind, b the buoyancy, f_0 the Coriolis factor, N the Brünt–Vaisala frequency, and $\mathbf{i}$, $\mathbf{j}$, and $\mathbf{k}$ the unit vectors of our coordinates system. D accounts for all diabatic forcing. Moist formulations of the Eliassen–Palm diagnostics have been designed and discussed in the literature to include diabatic processes and have proven to predict regions of intense wave activity more accurately in moist atmospheres, but they lack a theoretical set of equations to explain the exchanges between the waves and the mean flow (Dwyer & O'Gorman, 2017), which is what we are interested in here. Hence, diabatic processes are kept included in term D for this analysis. The divergence of the Eliassen–Palm vector $\mathcal{F}$ can be found on the right-hand side of the energy budget for the mean flow; for instance, see Dwyer and O'Gorman (2017, eq. 3). Thus, the equation of Eliassen–Palm can be interpreted as follows. When the divergence of the Eliassen–Palm vector is positive, the wave loses energy to the mean flow. On the other hand, when the divergence of the Eliassen–Palm vector is negative, the mean flow loses energy to the wave. Locally, the Eliassen–Palm vector is a proxy of the energy transported by the wave. To apply the Eliassen–Palm decomposition in the MTZ, we integrate zonally between 18°W and 42°W instead of the whole globe. Consequently, two steps of the derivation have to be revised. In our three cases, the error on the simplification of the budget of q' due to the partial zonal integration ranges between 1.1% and 4.6%, which is deemed reasonable in the following. However, in the final steps of the derivation, a corrective term has to be taken into account. The corrected Eliassen–Palm equation that can be applied in the MTZ is written as follows:

$$\frac{\partial A}{\partial t} + \nabla \mathcal{F} + C = D, \tag{4}$$

$$C = \frac{1}{2}\left[(v'^2 - u'^2) - \frac{b'^2}{N^2}\right]_{x_2}^{x_1}, \tag{5}$$

where x_1 is the westernmost zonal coordinate of the MTZ and x_2 its easternmost zonal coordinate. C also appears in the right-hand side of the energy budget of the mean flow. Therefore, the interpretation of $\nabla\mathcal{F} + C$ is analogous to that of $\nabla\mathcal{F}$ in the regular case. The zonal extension of the MTZ being of the same order of magnitude than AEW-S wavelength means a small signature of the AEW may persist in the mean flow. To minimize this source of error, for each trough, we average $\nabla\mathcal{F} + C$ over the time of residence of the wave trough inside the MTZ.

Results are shown on the left panels of Figure 8 for the AEWs-S associated with *Pierre-Henri*, *Peter*, and *Rose*. At the level of the AEJ, the mean flow benefits from the interaction with the wave for the three events. This is consistent with the weakening of the relative vorticity at jet level along *Rose*'s trajectory. For *Rose* and *Pierre-Henri*, the interaction with the mean flow is mostly beneficial in the low troposphere, consistent with the development of the circulation at low level (see right panel), before and immediately after the entry in the MTZ. Between 700 and 900 hPa the Eliassen–Palm flux is mainly downwards and southward out of the AEJ core, decreasing vertical gradients of vorticity, consistent with the development of the circulation. On the other hand, for the AEW-S associated with *Peter*, the interaction between the wave and the mean flux is mainly detrimental to the wave. A reformation of the MTZ is shown in Figure 7 on the passage of the AEW-S: the energy taken up from the wave might explain that the trade winds are restored east of the wave center on September 15. At 12.5°N (the mean latitude of the trough inside the MTZ), the Eliassen–Palm fluxes are almost null. The vertical profile of relative vorticity shows a consistent decrease of relative vorticity at all pressure levels after a noticeable vertical extension before the entry into the MTZ. There is no signature of any intensification of the low-level circulation inside the MTZ. This detrimental interaction might explain why *Peter* failed to develop in this part of the basin (and developed much further west) even though the circulation at jet level was well organized (according to the NHC report). The Eliassen–Palm analysis confirms what has been hypothesized looking at the evolution of the low-level circulation.

6 | AEW-N–AEW-S INTERACTIONS

Peter did not benefit from a positive energy flux from either the AEJ or from the monsoon, but it eventually developed in the west half of the basin. On the other hand, the interaction between the AEW-S associated with *Pierre-Henri* and the MTZ was positive, favoring the creation of a coherent vortex over the column; but as the pouch formed, it encompassed dry air that might explain the collapse of the circulation. To try to explain those two events, we look at the interaction between the AEW-S and the AEW-N during the month of September 2021. As explained in Section 3, our analysis benefits from the

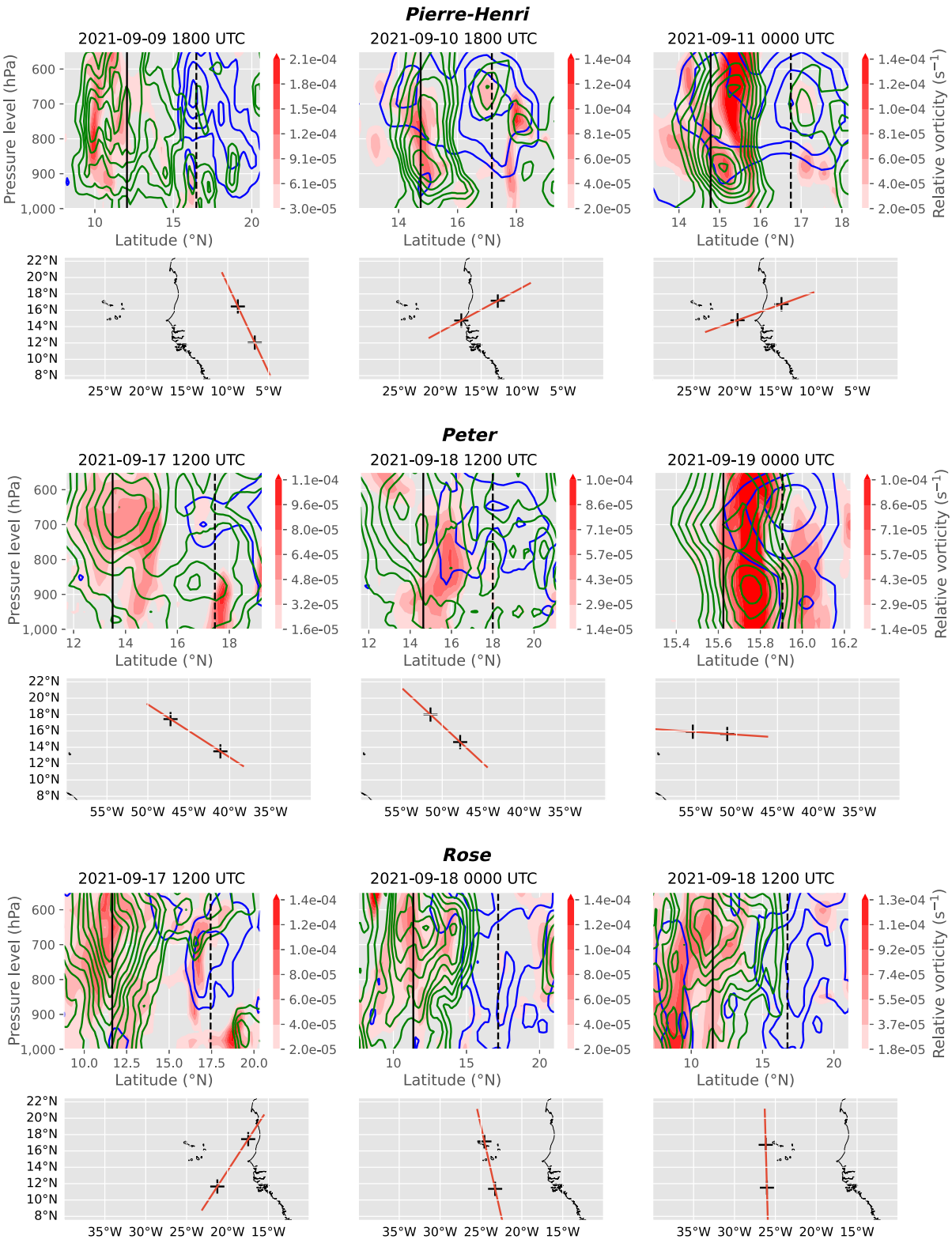

FIGURE 9 Lower panels: Each cross represent the tracked location of an African easterly wave (AEW)-S or AEW-N center, and the red line represents the transect for which the vertical cut is plotted in the upper panels. Upper panels: Unfiltered relative vorticity (shading), relative vorticity filtered on the period window 2–4.4 days (green contours, one isoline each 5×10^{-6} s^{-1}), and relative vorticity filtered on the period window 4.4–7 days (blue contours, one isoline each 5×10^{-6} s^{-1}); the continuous black line represents the tracked location of the AEW-S, and the dashed black line is the tracked location of the AEW-N.

fact that in September 2021 the spectral characteristics of each wave track are separated. The vorticity maximum in the period scale 4.4–7 days is tracked and the trajectories displayed in Figure 6.

Figure 9 shows vertical cuts of vorticity profiles as vortices on each side of the jet evolve. The lower panels locate the two vortex centers and the location of the transect plotted in the upper panels. For *Pierre-Henri* and *Peter*, an interaction between the two wave tracks can be observed: the isolines of filtered vorticity get entangled and the unfiltered vorticity moves from being centered on the AEW-S vorticity maxima (*Peter*, left panel) or south of the AEW-S vorticity maxima (*Pierre-Henri*, left panel) to a location in between the AEW-S and AEW-N centers. This evolution goes with an increase of unfiltered vorticity in the regions where AEW-S and AEW-N activity are collocated. For *Pierre-Henri*, this interaction seem to be at play mainly in the midtroposphere and fails to structure a vertically aligned vortex (on September 11, 0000 UTC, the most intense vortex in the unfiltered signal is vertically tilted). For *Peter*, this interaction leads to the formation of a vertically coherent and intense vortex in the whole column. The development of a coherent vortex before TC genesis is consistent with the necessary condition formulated by Wang et al., (2012). For *Rose*, on the other hand, the structures of the two waves are not collocated and remain independent before the genesis. The vertical development of the vortex happens southward of the AEW-S center, supporting the idea that the development is not related to the AEW-S–AEW-N interaction. The development is observed at the latitude where the maximum low vorticity was observed in relation to the MTZ, consistent with the findings of the previous section.

In accordance with the findings discussed in Section 4, *Pierre-Henri* develops a pouch structure, which notably includes dusty air that could potentially act as a marker for the SAL. As has been put forward by Grogan and Thorncroft (2019), AEW troughs can transport SAL on the north flank of the AEJ. This interaction between AEW-N and AEW-S might elucidate the reason behind the incorporation of SAL within *Pierre-Henri*'s pouch structure. Figure 10 shows the circulation at 850 hPa and the AEW-S and AEW-N wave troughs. The low-level circulation was closed around the AEW-S trough on September 9 at 1800 UTC. But as the AEW-S trough gets closer to the AEW-N trough, the northeastern quadrant flow is first diverted into two branches: one that circles around the AEW-S trough as before, and one that circles around the AEW-N trough on September 10 at 0600 UTC. The low-level circulation closes again to finally encompass the northern trough on September 10 at 1800 UTC. But north of the AEJ, SAL can be found (low water vapor content, Figure 10, and high dust concentration, Figure 4). Therefore, when the circulation closes to encompass the two troughs, dry air is advected inside the circulation (visible -n the northwestern quadrant of the circulation at 1800 UTC on September 10). The convective cores identified with brightness temperature (not shown here) are less numerous on September 11, and the campaign flights have also shown weaker convective activity in the system than expected. The presence of dry air inside the pouch might explain why *Pierre-Henri* failed to develop into a TC.

7 | DYNAMICAL MODULATION OF DUST ASSIMILATION

In the previous section, we discussed the dynamical processes that played a role in the development or collapse of the three AEW events sampled during CADDIWA.

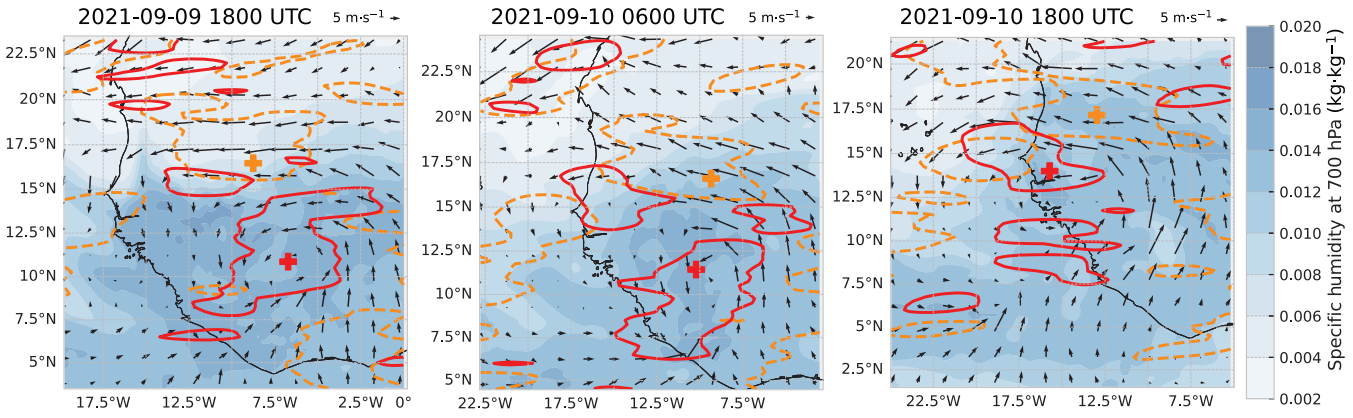

FIGURE 10 Shading: Specific humidity at 850 hPa ($kg \cdot kg^{-1}$). Solid red contour: $1.5 \times 10^{-5}\,s^{-1}$ contour line of 2–4.4 days filtered relative vorticity at 700 hPa. Dashed orange contour: $7.5 \times 10^{-6}\,s^{-1}$ contour line of 4.4–7 days filtered relative vorticity at 700 hPa. Vectors: wind at 850 hPa. The red (orange) cross marks the location of the center of the troughs of the AEW-S (AEW-N) associated with *Pierre-Henri*.

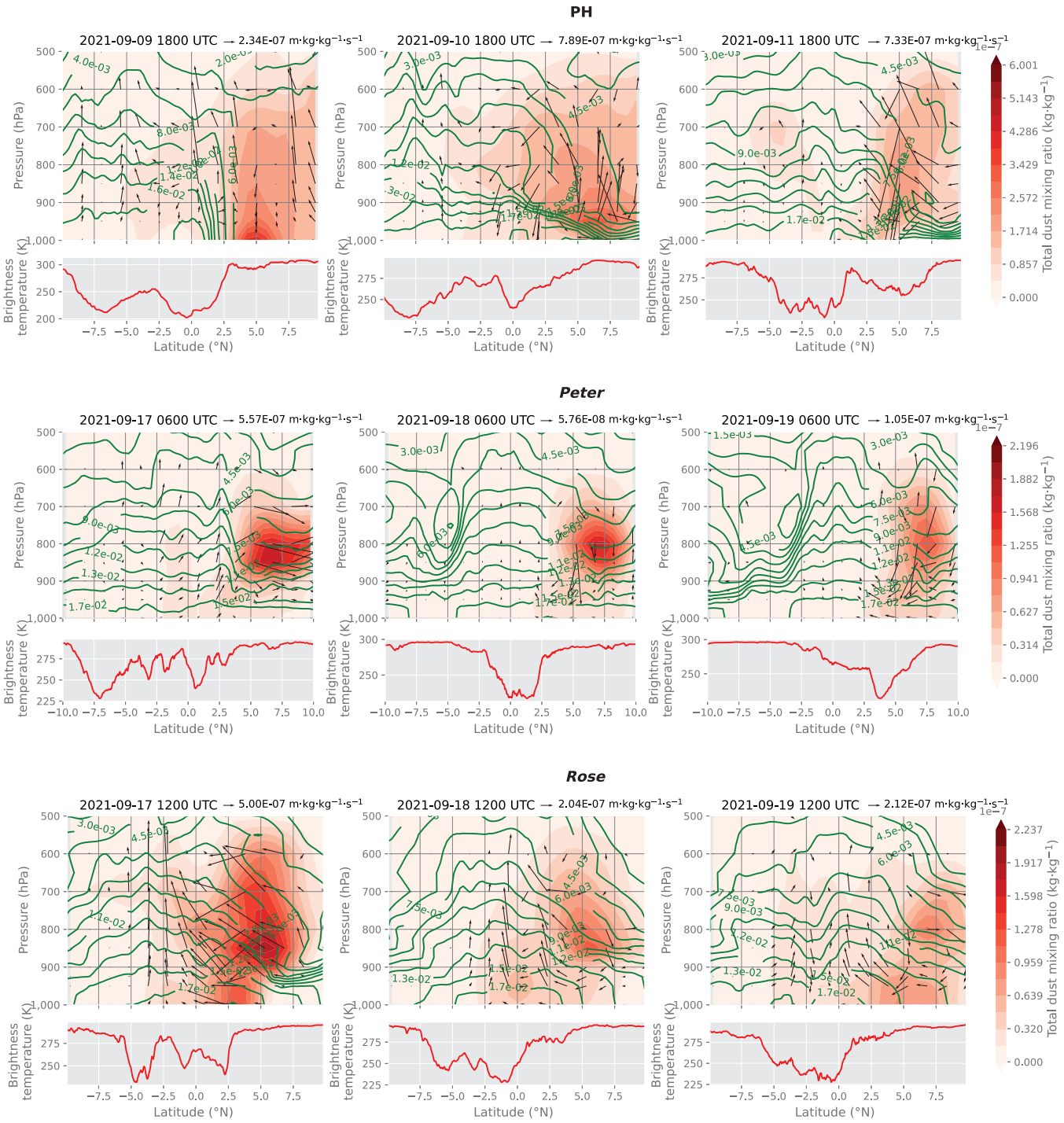

FIGURE 11 Top panels: Dust concentration (in shading), specific humidity (kg·kg^{-1}; green contours), dust fluxes in the frame of reference of the mesoscale convective system (MCS; vectors; the vertical component has been multiplied by a factor 50 for the sake of readability). Bottom panels: Brightness temperature (K). Figures replicated for the main MCS associated with *Pierre-Henri* (PH; top), *Peter* (middle), and *Rose* (bottom). Each quantity has been averaged over ±2 ° of longitude.

To pave the way for further studies on the cloud–atmospheric dynamics–dust interaction, we focus in this section on the impacts of the dynamical processes discussed in this article on dust concentration and transport. Dust mixing ratios at 700 hPa are shown in Figures 4 and 5. All the processes previously discussed happen south of the AEJ that separated the humid air from the drier SAL in the north. However, convective systems seem to develop close to dust concentration contour lines.

In the following, we take a closer look at the tracking of the main MCS identified for each AEW trough and the dust transport in the frame of reference of the MCS. Figure 11

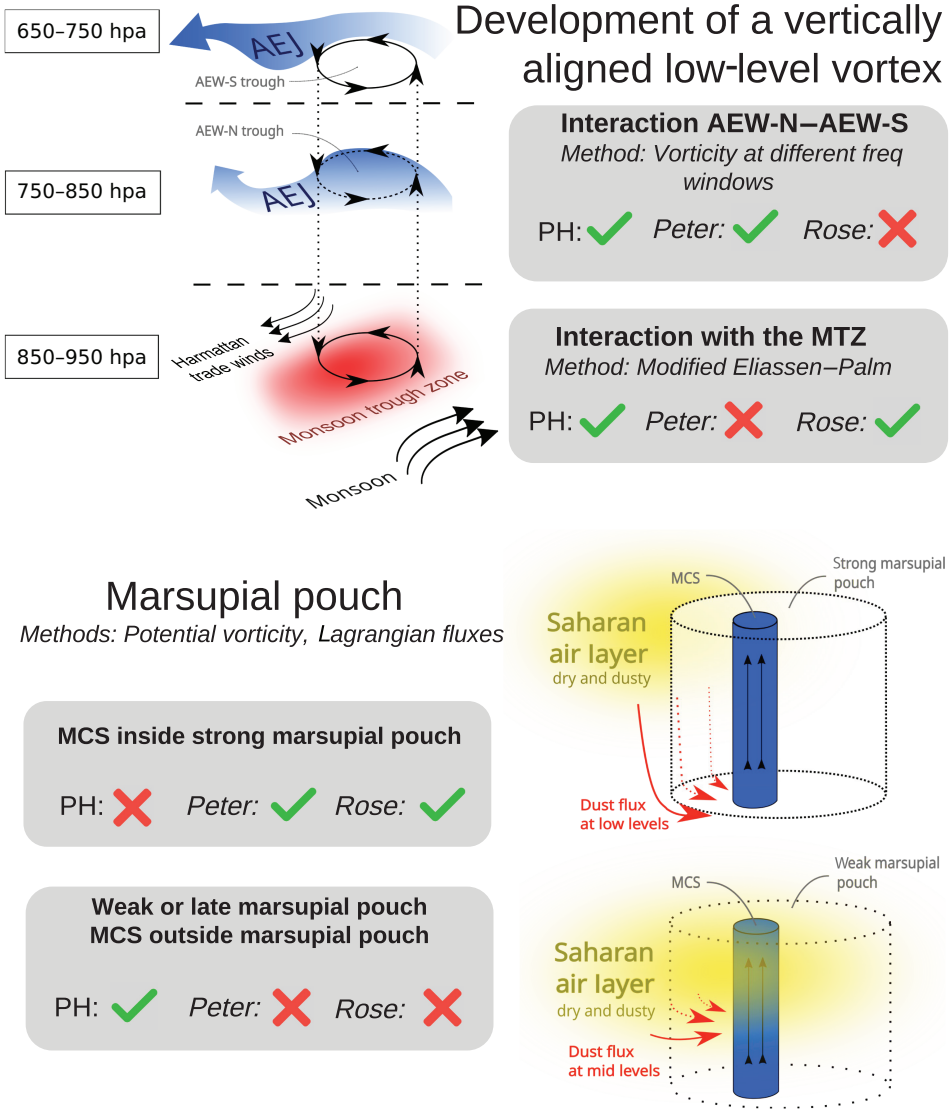

FIGURE 12 Summary of the processes investigated throughout this study, the methods used, and the key findings for each African easterly wave (AEW) event. For each process discussed in the article, a conceptual scheme is shown. Next to each event, there is a green tick when the process has been observed and discussed and a red cross when it has not. AEJ, African easterly jet; MCS, mesoscale convective system; MTZ, monsoon trough zone; PH, *Pierre-Henri*.

shows the dust transport (vectors), the specific humidity, dust concentration, and brightness temperature averaged over ±2 ° of longitude. Low brilliance temperature helps to locate the convective cores. For *Pierre-Henri*, from September 10 on, intrusions of dust and dry air inside the convective core at 13°N can be observed at all levels. This is consistent with the lack of a structured pouch before September 2011. The SAL intrudes the trough-related circulation, inhibiting further developments. For *Peter* and *Rose*, on the other hand, no dust is transported inside the convective core above 900 hPa, supporting the idea of the protecting pouches. However, dust is incorporated inside the MCS by the low-level circulation. This mass of air is in contact with the ocean and benefits from the surface flux of water vapor: for *Peter* and *Rose*, the dust mixing ratio increases north of the convective core in the lower layers, with no impact on specific water content. The SAL might, therefore, get moistened and this process might counteract the drying effect of SAL incorporation observed in the case of *Pierre-Henri*.

The effect of the dust once incorporated still has to be investigated. Rosenfeld et al. (2012) have put forward the idea that aerosols acting as cloud condensation nuclei in the peripheral clouds might increase peripheral convection to the detriment of the eyewall convection, leading to a decrease in intensity of the TC overall. On the other hand, Hoarau (2018) has shown by coupling a model of sea-salt aerosol generation with a circulation model that incorporating aerosol from below the circulation increases convection in the whole system, eyewall included. The way dust is incorporated in the system might thus play a role in the cyclogenetic process and should be subject to further research.

8 | CONCLUSION

The three AEWs sampled during the CADDIWA campaign were studied using ERA5 and CAMS reanalysis and MERGED-IR satellite data. In September 2021, there

was a favorable area of TC formation slightly displaced to the south compared with the climatology but of the same magnitude overall. The AEWs in September 2021 are characterized by two distinct spectral peaks for the wave tracks on each side of the AEJ. During the time span of the campaign, three AEW-S troughs and two AEW-N troughs exited the continent. Our key findings and the conceptual framework developed in previous sections are summed up in Figure 12: the top panel shows how the interaction between AEW-S and AEW-N, on the one hand (*Pierre-Henri*, *Peter*), and with the MTZ (*Pierre-Henri*, *Rose*), on the other hand, helps to develop a coherent vortex in the whole troposphere; the lower panel shows how a strong wave pouch (*Peter*, *Rose*) protects convective systems from dry-air intrusion and modulates dust fluxes.

The presence of cyclonic preconditioning at low levels associated with the MTZ has been highlighted, consistent with the literature (Arnault & Roux, 2011). *Pierre-Henri* and *Rose* benefited from that interaction. *Rose*developed a vertically coherent vortex in the whole column helped by an intense low-level vorticity associated with the MTZ. On the other hand, *Peter* did not benefit from the interaction with the MTZ. The presence of a very active Saharan heat low close to the coast weakened the meriodional gradients of zonal wind and the associated low-level vorticity. The use of a modified Eliassen–Palm diagnostic to quantify the interaction between AEWs and the monsoon has proven useful and may be extended to a climatology of AEW to better understand the different interaction processes.

Peter did not benefit from its interaction with the MTZ but was provided low-level vorticity by an AEW-N on the western side of the basin (see "Development of a vertically aligned low-level vortex", Figure 12). *Pierre-Henri* also benefited from such an interaction over the continent, resulting in a peak in kinetic energy (not shown). However, the interaction with an AEW-N brought dry air into the circulation that might partly explain the decay of *Pierre-Henri*. The structure of *Pierre-Henri* is comparable to the non-developing wave observed by Brammer et al. (2018), with dry air in the midtroposphere and a vertically tilted vortex. The potential of AEW-N–AEW-S interaction to explain this type of structure requires further investigations. To our knowledge, this type of interaction between AEWs has not been discussed in the literature to date.

In our study of AEW-N–AEW-S interaction, we took advantage of the fact that two separate spectral peaks were identified in association with each vortex track in September 2021. The spectral characteristics differences between AEW-N and AEW-S in the climatology will be studied in further research to assess the possibility of generalizing this type of analysis.

The interactions between the AEWs and the convection have been studied within the marsupial paradigm framework (see "Marsupial pouch", Figure 12): the circulation induced by the wave in the midtroposphere protects convective systems collocated with the trough. Using both PV and streamlines in the frame of reference of AEWs troughs, we highlighted the existence of a Kelvin cat's eye (e.g., quasi-closed streamlines in the reference frame of the wave) that protected the convective system from the intrusion of the SAL inside the circulation. When the pouch fails to develop early enough and encloses part of the SAL (as in the case of *Pierre-Henri*), or when convective systems develop out of a pouch, they were found to have shorter life span and dissipate quickly. On the other hand, the two protected MCSs eventually developed into TS *Peter* and TS *Rose*.

Finally, the presence of a flux of dust near the surface and toward the center of the convective system has been highlighted for both *Rose* and *Peter* (see "Marsupial pouch", Figure 12). The role of this dust in the intensification of the systems still has to be investigated using a modeling approach and in-situ data from the campaign and could provide insights to better understand the microphysics of TC genesis in the North Atlantic basin.

ACKNOWLEDGEMENTS

The airborne component of CADDIWA was supported by the French national program LEFE/INSU of the Centre National de la Recherche Scientifique (CNRS), Centre National d'Etudes Spatiales (CNES), the European Space Agency (ESA), and the Institut Pierre-Simon Laplace (IPSL). The CNES/TOSCA projects funding these activities are called CADDIWA and IASI – Aerosols. Airborne data were obtained using the aircraft managed by Safire, the French facility for airborne research, an infrastructure of the French National Center for Atmospheric Research (CNRS), Météo-France, and the French National Center for Space Studies (CNES). Tanguy Jonville acknowledges the French Ministry for the Environmental Transition (MTECT) for the funding of his PhD. We thank the anonymous reviewers for their comments and suggestions that have greatly improved the article.

DATA AVAILABILITY STATEMENT

Data available on request from the authors.

ORCID

Tanguy Jonville https://orcid.org/0009-0004-8430-0285

REFERENCES

Arnault, J. & Roux, F. (2010) Comparison between two case studies of developing and nondeveloping African easterly waves during NAMMA and AMMA/SOP-3: absolute vertical vorticity budget. *Monthly Weather Review*, 138(4), 1420–1445.

Arnault, J. & Roux, F. (2011) Characteristics of African easterly waves associated with tropical cyclogenesis in the Cape Verde Islands region in July-August-September of 2004-2008. *Atmospheric Research*, 100(1), 61–82.

Asaadi, A., Brunet, G. & Yau, M.K. (2016a) On the dynamics of the formation of the kelvin Cat's-eye in tropical cyclogenesis. Part I: climatological investigation. *Journal of the Atmospheric Sciences*, 73(6), 2317–2338.

Asaadi, A., Brunet, G. & Yau, M.K. (2016b) On the dynamics of the formation of the kelvin Cat's-eye in tropical cyclogenesis. Part II: numerical simulation. *Journal of the Atmospheric Sciences*, 73(6), 2339–2359.

Asaadi, A., Brunet, G. & Yau, M.K. (2017) The importance of critical layer in differentiating developing from nondeveloping easterly waves. *Journal of the Atmospheric Sciences*, 74(2), 409–417.

Baklanov, A., Brunner, D., Carmichael, G., Flemming, J., Freitas, S., Gauss, M. et al. (2018) Key issues for seamless integrated chemistry–meteorology modeling. *Bulletin of the American Meteorological Society*, 98, 2285–2292.

Bock, O., Bosser, P., Flamant, C., Doerflinger, E., Jansen, F., Fages, R. et al. (2021) Integrated water vapour observations in the Caribbean arc from a network of ground-based GNSS receivers during EUREC^{4}A. *Earth System Science Data*, 13(5), 2407–2436.

Brammer, A. & Thorncroft, C.D. (2015) Variability and evolution of African easterly wave structures and their relationship with tropical cyclogenesis over the eastern Atlantic. *Monthly Weather Review*, 143(12), 4975–4995.

Brammer, A., Thorncroft, C.D. & Dunion, J.P. (2018) Observations and predictability of a nondeveloping tropical disturbance over the eastern Atlantic. *Monthly Weather Review*, 146(9), 3079–3096.

Burpee, R.W. (1972) The origin and structure of easterly waves in the lower troposphere of North Africa. *Journal of the Atmospheric Sciences*, 29(1), 77–90.

Chen, T.C. (2006) Characteristics of African easterly waves depicted by ECMWF reanalyses for 1991–2000. *Monthly Weather Review*, 134(12), 3539–3566.

Chen, T.C., Wang, S.Y. & Clark, A.J. (2008) North Atlantic hurricanes contributed by African easterly waves north and south of the African easterly jet. *Journal of Climate*, 21(24), 6767–6776.

Cornforth, R.J., Hoskins, B.J. & Thorncroft, C.D. (2009) The impact of moist processes on the African easterly jet–African easterly wave system. *Quarterly Journal of the Royal Meteorological Society*, 135(641), 894–913.

Danso, D.K., Patricola, C.M. & Bercos-Hickey, E. (2022) Influence of African easterly wave suppression on Atlantic tropical cyclone activity in a convection-permitting model. *Geophysical Research Letters*, 49(22), e2022GL100590.

Diaz, M. & Aiyyer, A. (2013) Energy dispersion in African easterly waves. *Journal of the Atmospheric Sciences*, 70(1), 130–145.

Dunkerton, T.J., Montgomery, M.T. & Wang, Z. (2009) Tropical cyclogenesis in a tropical wave critical layer: easterly waves. *Atmospheric Chemistry and Physics*, 9(15), 5587–5646.

Duvel, J.P. (2021) On vortices initiated over West Africa and their impact on North Atlantic tropical cyclones. *Monthly Weather Review*, 149(2), 585–601.

Dwyer, J.G. & O'Gorman, P.A. (2017) Moist formulations of the Eliassen–Palm flux and their connection to the surface westerlies. *Journal of the Atmospheric Sciences*, 74(2), 513–530.

Edmon, H.J., Hoskins, B.J. & McIntyre, M.E. (1980) Eliassen-Palm cross sections for the troposphere. *Journal of the Atmospheric Sciences*, 37(12), 2600–2616.

Emanuel, K. (2001) Contribution of tropical cyclones to meridional heat transport by the oceans. *Journal of Geophysical Research: Atmospheres*, 106(D14), 14771–14781.

Enyew, B.D. & Mekonnen, A. (2022) The interaction between African easterly waves and different types of deep convection and its influence on Atlantic tropical cyclones. *Atmosphere*, 13(1), 5.

Fan, J., Wang, Y., Rosenfeld, D. & Liu, X. (2016) Review of aerosol–cloud interactions: mechanisms, significance, and challenges. *Journal of the Atmospheric Sciences*, 73(11), 4221–4252.

Fink, A.H. & Reiner, A. (2003) Spatiotemporal variability of the relation between African easterly waves and West African squall lines in 1998 and 1999. *Journal of Geophysical Research: Atmospheres*, 108(D11), 4332.

Flamant, C., Chaboureau, J.P., Delanoë, J., Gaetani, M., Jamet, C., Lavaysse, C. et al. (2024) Cyclogenesis in the tropical Atlantic: first scientific highlights from the clouds-atmospheric dynamics-dust interactions in West Africa (CADDIWA) field campaign. *Bulletin of the American Meteorological Society*, 105, E387–E417.

Flamant, C., Delanoë, J., Chaboureau, J.P., Lavaysse, C., Gaetani, M. & Bock, O. (2021) La campagne Caddiwa dans la région des îles du cap-vert. *La Météorologie*, 115, 2–5.

Grogan, D.F.P., Nathan, T.R. & Chen, S.H. (2016) Effects of Saharan dust on the linear dynamics of African easterly waves. *Journal of the Atmospheric Sciences*, 73(2), 891–911.

Grogan, D.F.P., Nathan, T.R. & Chen, S.H. (2019) Structural changes in the African easterly jet and its role in mediating the effects of Saharan dust on the linear dynamics of African easterly waves. *Journal of the Atmospheric Sciences*, 76(11), 3351–3365.

Grogan, D.F.P. & Thorncroft, C.D. (2019) The characteristics of African easterly waves coupled to Saharan mineral dust aerosols. *Quarterly Journal of the Royal Meteorological Society*, 145(720), 1130–1146.

Hankes, I., Wang, Z., Zhang, G. & Fritz, C. (2015) Merger of African easterly waves and formation of Cape Verde storms. *Quarterly Journal of the Royal Meteorological Society*, 141(689), 1306–1319.

Herbener, S.R., van den Heever, S.C., Carrió, G.G., Saleeby, S.M. & Cotton, W.R. (2014) Aerosol indirect effects on idealized tropical cyclone dynamics. *Journal of the Atmospheric Sciences*, 71(6), 2040–2055.

Hersbach, H., Bell, B., Berrisford, P., Hirahara, S., Horányi, A., Muñoz-Sabater, J. et al. (2020) The ERA5 global reanalysis. *Quarterly Journal of the Royal Meteorological Society*, 146(730), 1999–2049.

Hoarau, T. (2018) *Couplage Aérosols-microphysique pour La simulation des cyclones Tropicaux: Cas Du cyclone Dumile (2013)*. [These de doctorat] La Réunion.

Inness, A., Ades, M., Agustí-Panareda, A., Barré, J., Benedictow, A., Blechschmidt, A.M. et al. (2019) The CAMS reanalysis of atmospheric composition. *Atmospheric Chemistry and Physics*, 19(6), 3515–3556.

Janiga, M.A. & Thorncroft, C.D. (2013) Regional differences in the kinematic and thermodynamic structure of African easterly waves. *Quarterly Journal of the Royal Meteorological Society*, 139(675), 1598–1614.

Janowiak, J., Joyce, B. & Xie, P. (2017) *NCEP/CPC L3 half hourly 4km global (60S - 60N) merged IR V1*. Goddard Earth Sciences Data and Information Services Center (GES DISC).

Jenkins, M.A. (1995) The cold-core temperature structure in a tropical easterly wave. *Journal of the Atmospheric Sciences*, 52(8), 1168–1177.

Jones, C., Mahowald, N. & Luo, C. (2004) Observational evidence of African desert dust intensification of easterly waves. *Geophysical Research Letters*, 31(17), L17208.

Jury, M.R. & Santiago, M.J. (2010) Composite analysis of dust impacts on African easterly waves in the moderate resolution imaging spectrometer era. *Journal of Geophysical Research: Atmospheres*, 115(D16), D16213.

Knippertz, P. & Todd, M.C. (2010) The central west Saharan dust hot spot and its relation to African easterly waves and extratropical disturbances. *Journal of Geophysical Research: Atmospheres*, 115(D12), D12117.

Kwon, H.J. & Mak, M. (1990) A study of the structural transformation of the African easterly waves. *Journal of the Atmospheric Sciences*, 47(3), 277–292.

Landsea, C.W. & Franklin, J.L. (2013) Atlantic hurricane database uncertainty and presentation of a new database format. *Monthly Weather Review*, 141(10), 3576–3592.

Lavaysse, C., Flamant, C., Janicot, S. & Knippertz, P. (2010) Links between African easterly waves, midlatitude circulation and intraseasonal pulsations of the West African heat low. *Quarterly Journal of the Royal Meteorological Society*, 136(S1), 141–158.

Lee, G.R., Gommers, R., Waselewski, F., Wohlfahrt, K. & O'Leary, A. (2019) PyWavelets: a python package for wavelet analysis. *Journal of Open Source Software*, 4(36), 1237.

Leppert, K.D., Cecil, D.J. & Petersen, W.A. (2013) Relation between tropical easterly waves, convection, and tropical cyclogenesis: a Lagrangian perspective. *Monthly Weather Review*, 141(8), 2649–2668.

Leroux, S., Hall, N.M.J. & Kiladis, G.N. (2010) A climatological study of transient–mean-flow interactions over West Africa. *Quarterly Journal of the Royal Meteorological Society*, 136(S1), 397–410.

Liu, Y., Liang, X.S. & Weisberg, R.H. (2007) Rectification of the bias in the wavelet power spectrum. *Journal of Atmospheric and Oceanic Technology*, 24(12), 2093–2102.

Mekonnen, A., Thorncroft, C.D. & Aiyyer, A.R. (2006) Analysis of convection and its association with African easterly waves. *Journal of Climate*, 19(20), 5405–5421.

Menkes, C.E., Lengaigne, M., Marchesiello, P., Jourdain, N.C., Vincent, E.M., Lefèvre, J. et al. (2012) Comparison of tropical cyclogenesis indices on seasonal to interannual timescales. *Climate Dynamics*, 38(1), 301–321.

Montgomery, M.T., Davis, C., Dunkerton, T., Wang, Z., Velden, C., Torn, R. et al. (2012) The pre-depression investigation of cloud-systems in the tropics (PREDICT) experiment: scientific basis, new analysis tools, and some first results. *Bulletin of the American Meteorological Society*, 93(2), 153–172.

Montgomery, M.T., Wang, Z. & Dunkerton, T.J. (2010) Coarse, intermediate and high resolution numerical simulations of the transition of a tropical wave critical layer to a tropical storm. *Atmospheric Chemistry and Physics*, 10(22), 10803–10827.

N'Datchoh, E.T., Diallo, I., Konaré, A., Silué, S., Ogunjobi, K.O., Diedhiou, A. et al. (2018) Dust induced changes on the west African summer monsoon features. *International Journal of Climatology*, 38(1), 452–466.

Nathan, T.R., Grogan, D.F.P. & Chen, S.H. (2019) Saharan dust transport during the incipient growth phase of African easterly waves. *Geosciences*, 9(9), 388.

Nowottnick, E.P., Colarco, P.R., Braun, S.A., Barahona, D.O., da Silva, A., Hlavka, D.L. et al. (2018) Dust impacts on the 2012 hurricane Nadine track during the NASA HS3 field campaign. *Journal of the Atmospheric Sciences*, 75(7), 2473–2489.

Ocasio, K.M.N., Brammer, A., Evans, J.L., Young, G.S. & Moon, Z.L. (2021) Favorable monsoon environment over eastern Africa for subsequent tropical cyclogenesis of African easterly waves. *Journal of the Atmospheric Sciences*, 78(9), 2911–2925.

Pan, B., Wang, Y., Hu, J., Lin, Y., Hsieh, J.S., Logan, T. et al. (2018) Impacts of Saharan dust on Atlantic regional climate and implications for tropical cyclones. *Journal of Climate*, 31(18), 7621–7644.

Patricola, C.M., Saravanan, R. & Chang, P. (2018) The response of Atlantic tropical cyclones to suppression of African easterly waves. *Geophysical Research Letters*, 45(1), 471–479.

Pytharoulis, I. & Thorncroft, C. (1999) The low-level structure of African easterly waves in 1995. *Monthly Weather Review*, 127(10), 2266–2280.

Reale, O., Lau, K.M., da Silva, A. & Matsui, T. (2014) Impact of assimilated and interactive aerosol on tropical cyclogenesis. *Geophysical Research Letters*, 41(9), 3282–3288.

Rosenfeld, D., Woodley, W.L., Khain, A., Cotton, W.R., Carrió, G., Ginis, I. et al. (2012) Aerosol effects on microstructure and intensity of tropical cyclones. *Bulletin of the American Meteorological Society*, 93(7), 987–1001.

Russell, J.O., Aiyyer, A., White, J.D. & Hannah, W. (2017) Revisiting the connection between African easterly waves and Atlantic tropical cyclogenesis. *Geophysical Research Letters*, 44(1), 587–595.

Rutherford, B., Boothe, M.A., Dunkerton, T.J. & Montgomery, M.T. (2018) Dynamical properties of developing tropical cyclones using Lagrangian flow topology. *Quarterly Journal of the Royal Meteorological Society*, 144(710), 218–230.

Saleeby, S.M., Herbener, S.R., van den Heever, S.C. & L'Ecuyer, T. (2015) Impacts of cloud droplet–nucleating aerosols on shallow tropical convection. *Journal of the Atmospheric Sciences*, 72(4), 1369–1385.

Seinfeld, J.H., Bretherton, C., Carslaw, K.S., Coe, H., DeMott, P.J., Dunlea, E.J. et al. (2016) Improving our fundamental understanding of the role of aerosol-cloud interactions in the climate system. *Proceedings of the National Academy of Sciences*, 113(21), 5781–5790.

Sun, Y. & Zhao, C. (2020) Influence of Saharan dust on the large-scale meteorological environment for development of tropical cyclone over North Atlantic Ocean basin. *Journal of Geophysical Research: Atmospheres*, 125(23), e2020JD033454.

Tang, B.H., Fang, J., Bentley, A., Kilroy, G., Nakano, M., Park, M.S. et al. (2020) Recent advances in research on tropical cyclogenesis. *Tropical Cyclone Research and Review*, 9(2), 87–105.

Thorncroft, C. & Hodges, K. (2001) African easterly wave variability and its relationship to Atlantic tropical cyclone activity. *Journal of Climate*, 14(6), 1166–1179.

Thorncroft, C.D. (1995) An idealized study of African easterly waves. III: more realistic basic states. *Quarterly Journal of the Royal Meteorological Society*, 121(527), 1589–1614.

Thorncroft, C.D., Hall, N.M.J. & Kiladis, G.N. (2008) Three-dimensional structure and dynamics of African easterly waves. Part III: genesis. *Journal of the Atmospheric Sciences*, 65(11), 3596–3607.

Tippett, M.K., Camargo, S.J. & Sobel, A.H. (2011) A Poisson regression index for tropical cyclone genesis and the role of large-scale vorticity in genesis. *Journal of Climate*, 24(9), 2335–2357.

Torrence, C. & Compo, G.P. (1998) A practical guide to wavelet analysis. *Bulletin of the American Meteorological Society*, 79(1), 61–78.

Tory, K.J., Dare, R.A., Davidson, N.E., McBride, J.L. & Chand, S.S. (2013) The importance of low-deformation vorticity in tropical cyclone formation. *Atmospheric Chemistry and Physics*, 13(4), 2115–2132.

Vallis, G.K. (2017) *Atmospheric and oceanic fluid dynamics: fundamentals and large-scale circulation*, 2nd edition. Cambridge, UK: Cambridge University Press.

Wang, Z., Dunkerton, T.J. & Montgomery, M.T. (2012) Application of the marsupial paradigm to tropical cyclone formation from northwestward-propagating disturbances. *Monthly Weather Review*, 140(1), 66–76.

Wang, Z. & Hankes, I. (2014) Characteristics of tropical easterly wave pouches during tropical cyclone formation. *Monthly Weather Review*, 142(2), 626–633.

Wang, Z., Montgomery, M.T. & Dunkerton, T.J. (2010a) Genesis of pre–hurricane Felix (2007). Part I: the role of the easterly wave critical layer. *Journal of the Atmospheric Sciences*, 67(6), 1711–1729.

Wang, Z., Montgomery, M.T. & Dunkerton, T.J. (2010b) Genesis of pre–hurricane Felix (2007). Part II: warm core formation, precipitation evolution, and predictability. *Journal of the Atmospheric Sciences*, 67(6), 1730–1744.

Wang, Z., Montgomery, M.T. & Fritz, C. (2012) A first look at the structure of the wave pouch during the 2009 PREDICT–GRIP dry runs over the Atlantic. *Monthly Weather Review*, 140(4), 1144–1163.

SUPPORTING INFORMATION

Additional supporting information can be found online in the Supporting Information section at the end of this article.

How to cite this article: Jonville, T., Flamant, C. & Lavaysse, C. (2024) Dynamical study of three African Easterly Waves in September 2021. *Quarterly Journal of the Royal Meteorological Society*, 1–21. Available from: https://doi.org/10.1002/qj.4720